ELSEVIER

Physica D 124 (1998) 285–295

PHYSICA D

An *elastica* problem: instabilities of an elastic arch

P. Patrício *, M. Adda-Bedia [2], M. Ben Amar [3]

Laboratoire de Physique Statistique[1] *de l'Ecole Normale Supérieure, 24 rue Lhomond, 75231 Paris Cedex 05, France*

Received 18 March 1998; accepted 3 July 1998
Communicated by H. Müller-Krumbhaar

Abstract

We analyze the modes of instability of an elastic homogeneous arch that is loaded at its center. We study first the dynamical linear stability of the symmetric elastic arch with respect to small perturbations. We also perform a constrained minimization of the static energy of the system. The numerical resolution of both the dynamical and the static problems allows the determination of the phase diagram corresponding to the behavior of the arch. For this simple *elastica* problem, the phase diagram shows a very rich structure that is in agreement with the experimental results. © 1998 Elsevier Science B.V.

PACS: 46.30.Lx 03.40.Dz 46.20.+e
Keywords: Elastica; Nonlinear dynamics; Instabilities; Energy minimization

1. Introduction

Several years ago, Pippard [1] has performed experiments on an elastic arch, loaded at its center, and fixed at both ends with an adjustable angle. He has shown that within this simple experiment, the modes of instability of the arch give rise to a rich phase diagram, which can be used as an illustration of catastrophe theory [2]. In this paper, we determine theoretically the phase diagram corresponding to Pippard's experiment [1] in the framework of the minimal elastic model of beams called the *elastica* [3]. This study provides a first step towards the understanding of the different instabilities that occur for large deformations of plates submitted to similar constraints [4,5].

As shown in Fig. 1, the experiment [1] is performed by fixing the extremities of an elastic homogeneous beam of length L and of a constant rectangular cross section of width a and thickness b. Typically, L is of the order of a meter, a of a centimeter, and b of a millimeter ($b < a \ll L$). The extremities of the beam are clamped at adjustable equal angles α and distance $l < L$. Finally, the system is loaded by a weight F at the mid-point of the beam.

When increasing quasi-statically the applied force F, it is observed that this system undergoes transitions between several configurations corresponding to different stable patterns of the arch: symmetric, plunged and asymmetric

* Corresponding author. E-mail: patricio@physique.ens.fr
[1] Laboratory associated with CNRS (URA 1306) and Universities Paris VI and Paris VII.
[2] E-mail: adda@physique.ens.fr
[3] E-mail: benamar@physique.ens.fr

PII: S0167-2789(98)00203-6

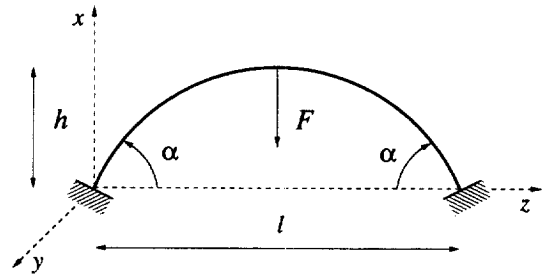

Fig. 1. Schematic representation of Pippard's experiment [1].

forms (see Fig. 5A, 5B and 5C, respectively). The main purpose of this work is to determine theoretically the corresponding phase diagram, using the elastic model described in Section 2.

In Section 2, we set down the nonlinear dynamical equations governing the motion of homogeneous elastic beams in the limit of a small strain, but possibly large displacements. We restrict ourselves to the case of the experiment [1], where an inextensible beam is submitted to a pure flexure [6–9] (lateral instabilities in the y-direction are prevented, at least until a certain limit, by the inequality $b < a$). Using these equations, we study in Section 3 the dynamical linear stability of the symmetric elastic arch with respect to small perturbations. This analysis gives the stability threshold with respect to symmetric and asymmetric perturbations around the symmetric arch. However, it does not allow to determine the stable shape towards which the arch tends to. In order to do this, we perform in Section 4 a constrained minimization of the static energy of the system. The numerical resolution of both the dynamical and the static problems allows the complete determination of the phase diagram corresponding to the behavior of the arch. Finally, the theoretical phase diagram is compared to the experimental one [1].

2. The elastic equations of a constrained arch

Suppose a homogeneous elastic body with a small maximal dimension of its cross section compared to its length (elastic *beam*). The theory of elasticity describes well the motion of this body under small local deformations. An elastic beam can perform large global deformations, remaining in the limits of this theory. The kinematics of the beam can be expressed in terms of an associated right-handed orthonormal local basis $\{\mathbf{d}_i\}$, $(i = 1, 2, 3)$.

The displacement of the beam at time t can be described by two equivalent representations (see Fig. 2). One can parametrize the three-dimensional body by $\mathbf{R}(\mathbf{x}, t)$, with $\mathbf{x} = (x, y, z)$. One can also associate to the beam a one-dimensional curve $\mathbf{r}(s \equiv z, t)$ together with two orthonormal vectors (the *directors*), $\mathbf{d}_1(s, t)$ and $\mathbf{d}_2(s, t)$, which represent the orientation of the cross section. The orientation of the elastic beam is preserved if $\mathbf{r}_{,s} \cdot \mathbf{d}_3 > 0$, $\mathbf{r}_{,s}$ represents the partial differentiation of $\mathbf{r}$ with respect to the variable s.

The classical elastic theory of Euler–Kirchhoff supposes that the motion of the cross section of coordinate s is undeformed and remains in the same plane of the local directors $\mathbf{d}_1$ and $\mathbf{d}_2$. This condition is written

$$\mathbf{R}(\mathbf{x}, t) = \mathbf{r}(s, t) + x\mathbf{d}_1(s, t) + y\mathbf{d}_2(s, t). \tag{1}$$

Furthermore, the theory prevents the neutral axis of the beam $\mathbf{r}(s, t)$ from suffering extension:

$$\mathbf{r}_{,s}(s, t) = \mathbf{d}_3(s, t). \tag{2}$$

The problem of Fig. 1 concerns a homogeneous beam submitted to a pure flexure. The domain of parameterization corresponding to the equilibrium configuration of this elastic beam is: $s \in [0, L]$ and $(x, y) \in [-b/2, b/2] \times$

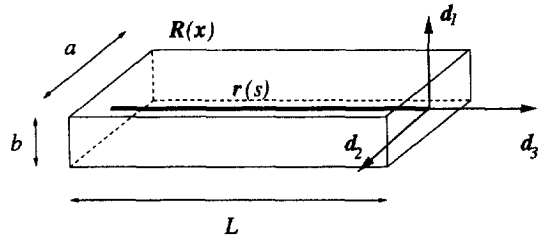

Fig. 2. Equilibrium configuration of the beam.

$[-a/2, a/2]$. We suppose that the deformation of the beam takes place in the plane xz. In fact, lateral instabilities in the y-direction are prevented, at least until a certain limit, by the inequality $b < a$.

Let $\theta(s,t)$ be the angle between the z-axis and the tangent to the beam at the coordinate s. Then, the tangent to the beam ($\mathbf{r}_{,s}$) and the orthonormal directors ($\mathbf{d}_1$ and $\mathbf{d}_2$) can be written as

$$\mathbf{d}_1(s,t) = \cos\theta(s,t)\mathbf{e}_x - \sin\theta(s,t)\mathbf{e}_z, \tag{3}$$

$$\mathbf{d}_2(s,t) = \mathbf{e}_y, \tag{4}$$

$$\mathbf{d}_3(s,t) = \mathbf{r}_{,s}(s,t) = \sin\theta(s,t)\mathbf{e}_x + \cos\theta(s,t)\mathbf{e}_z, \tag{5}$$

where $\mathbf{e}_x$, $\mathbf{e}_y$ and $\mathbf{e}_z$ are fixed normed vectors in the direction of x, y and z, respectively.

In these conditions, the elastic potential energy of the beam (also called in this case the Euler–Bernoulli beam) is given by [3]:

$$V_{\mathrm{el}}(t) = \frac{EJ}{2}\int_0^L \theta_{,s}^2(s,t)\,\mathrm{d}s, \tag{6}$$

where E is the Young Modulus and $J = ab^3/12$ is the second moment of the cross section. $\theta_{,s}^2$ is simply the square of the curvature of the elastic beam $\mathbf{r}(s,t)$. The kinetic energy of the beam, corresponding to the most important terms of the Rayleigh kinetic energy when the frequencies are small, is given by

$$T(t) = \frac{\rho}{2}\int_0^L A\mathbf{r}_{,t}^2(s,t)\,\mathrm{d}s, \tag{7}$$

where ρ is the mass density of the beam and $A = ab$ is the area of the cross section. Writing the position vector as $\mathbf{r} = r_x\mathbf{e}_x + r_z\mathbf{e}_z$, the energy exerted by the applied force is

$$V_F(t) = Fr_x(L/2,t) = F\int_0^{L/2} \sin\theta(s,t)\,\mathrm{d}s. \tag{8}$$

The boundary conditions are defined by imposing that the functions θ and $\theta_{,s}$ are continuous at $s = L/2$. Moreover, at $s = 0$ and $s = L$, the angles and positions of the elastic beam are both fixed. Defining $r_x(0,t) = 0$ and $r_z(0,t) = 0$, the boundary conditions reduce to

$$\theta(0,t) = \alpha, \qquad \theta(L,t) = -\alpha, \tag{9}$$

$$r_x(L,t) = \int_0^L \sin\theta(s,t)\,\mathrm{d}s = 0, \qquad r_z(L,t) = \int_0^L \cos\theta(s,t)\,\mathrm{d}s = l. \tag{10}$$

The equations of motion of the beam can be derived from a variational principle. The boundary conditions (10) are introduced in the variational problem with the help of two Lagrange multipliers $\lambda_1(t)$ and $\lambda_2(t)$. The action of this system is then defined by

$$\mathcal{A} = \int_{t_1}^{t_2} [T(t) - V_{\mathrm{el}}(t) - V_F(t) + \lambda_1(t) r_z(L,t) + \lambda_2(t) r_x(L,t)]\,\mathrm{d}t. \tag{11}$$

The equations of motion are obtained as the extremum of the action $\mathcal{A}$ with respect to variations of $\theta(s,t)$. If we introduce the functions n_x and n_z, such that

$$n_z(s,t) = \lambda_1(t) + \rho A \int_0^s r_{z,tt}(s',t)\,\mathrm{d}s', \tag{12}$$

$$n_x(s,t) = \lambda_2(t) - F/2 + \rho A \int_0^s r_{x,tt}(s',t)\,\mathrm{d}s' \quad \text{if } 0 \le s < L/2, \tag{13}$$

$$n_x(s,t) = \lambda_2(t) + F/2 + \rho A \int_0^s r_{x,tt}(s',t)\,\mathrm{d}s' \quad \text{if } L/2 < s \le L, \tag{14}$$

we obtain the well-known dynamical equations for an elastic homogeneous beam, subjected to a pure flexure [6]:

$$\rho A r_{x,tt}(s,t) = n_{x,s}(s,t), \tag{15}$$

$$\rho A r_{z,tt}(s,t) = n_{z,s}(s,t), \tag{16}$$

$$EJ\theta_{,ss}(s,t) = n_z(s,t)\sin\theta(s,t) - n_x(s,t)\cos\theta(s,t). \tag{17}$$

The functions n_x and n_z correspond to the contact forces exerted on the cross section of the beam. The addition of the pointlike force at the mid-point of the arch is taken into account by imposing a discontinuity of the contact force at $s = L/2$:

$$n_x^+(L/2,t) - n_x^-(L/2,t) = F, \tag{18}$$

where $n_x^+(L/2,t)(n_x^-(L/2,t))$ is the contact force of right (left) half of the arch at the point $s = L/2$.

The system is defined by the length L, the area A, the second moment J, the Young Modulus E and the mass density ρ. If L is taken as unit length, EJ/L^2 as unit force and $L^2\sqrt{\rho A/EJ}$ as unit time, one obtains the nondimensional equations

$$r_{x,tt}(s,t) = n_{x,s}(s,t), \tag{19}$$

$$r_{z,tt}(s,t) = n_{z,s}(s,t), \tag{20}$$

$$\theta_{,ss}(s,t) = n_z(s,t)\sin\theta(s,t) - n_x(s,t)\cos\theta(s,t). \tag{21}$$

We have derived the equations of motion of the elastica, starting from the definition of a Lagrangian. We would have obtained the same set of equations, by defining the constitutive equations that relates the shear deformations to the contact forces of the beam.

3. The symmetric solution and its linear stability analysis

Let us focus for the moment on the static problem. In this case, Eqs. (19) and (20) together with the condition (18) give

$$n_z(s) = \lambda_1, \tag{22}$$

$$n_x(s) = \lambda_2 - F/2 \quad \text{if } 0 \le s < 1/2, \tag{23}$$

$$n_x(s) = \lambda_2 + F/2 \quad \text{if } 1/2 < s \le 1. \tag{24}$$

Because there could be several asymmetrical solutions of the elastica equations, but only a few stable ones, we restrict ourselves to symmetric solutions around $s = 1/2$. So, we choose $\lambda_2 = 0$. Note that the first integral condition in (10) is automatically satisfied. Eq. (21) can be simplified to obtain

$$\theta_{,ss}(s) = \lambda_1 \sin\theta(s) + F/2 \cos\theta(s). \tag{25}$$

We have solved this equation numerically using a shooting method.[4] We have chosen as an input parameter the position of the mid-point $r_x(1/2) = h$ instead of F (see Fig. 1). Starting from $\theta(0) = \alpha$ and initial guesses for $\theta_{,s}(0)$, λ_1 and F, one integrates. Eq. (25) for $s \in [0, 1/2]$. Then using Newton's method, the guessed values are varied until the conditions $\theta(1/2) = 0$, $r_x(1/2) = h$ and $r_z(1/2) = l/2$ are statisfied with a sufficient accuracy. Once a particular solution is found, the convergence of the method is well achieved for all values α, l and h. Each solution is recursively found by using a previous one as initial guess. In fact, to each position h corresponds one symmetrical configuration, while a same force F can produce different configurations. The computations of these solutions are necessary in order to analyze the dynamic stability of the symmetric beam.

To study the stability of the symmetric shape of the beam, let us consider a dynamic perturbation around a static configuration

$$\theta(s,t) = \bar{\theta}(s) + \phi(s)\mathbf{e}^{\mathrm{i}wt}, \tag{26}$$

$$n_x(s,t) = \bar{n}_x(s) + f(s)\mathbf{e}^{\mathrm{i}wt}, \tag{27}$$

$$n_z(s,t) = \bar{n}_z(s) + g(s)\mathbf{e}^{\mathrm{i}wt}, \tag{28}$$

where $\bar{\theta}(s)$, $\bar{n}_x(s)$ and $\bar{n}_z(s)$ are the solutions of the static problem. $\phi(s)$, $f(s)$ and $g(s)$ are supposed to be small. If we replace these expressions in the equations of motion (19)–(21), retaining only linear terms in ϕ, f and g, we obtain

$$f_{,ss}(s) = -\omega^2\phi(s)\cos\bar{\theta}(s), \tag{29}$$

$$g_{,ss}(s) = \omega^2\phi(s)\sin\bar{\theta}(s), \tag{30}$$

$$\begin{aligned}\phi_{,ss}(s) = {} & \phi(s)(\bar{n}_x(s)\sin\bar{\theta}(s) + \bar{n}_z(s)\cos\bar{\theta}(s)) \\ & - f(s)\cos\bar{\theta}(s) + g(s)\sin\bar{\theta}(s).\end{aligned} \tag{31}$$

Finally, the boundary conditions (9) and (10) give

$$\phi(0) = \phi(1) = 0, \tag{32}$$

$$f_{,s}(0) = f_{,s}(1) = 0, \tag{33}$$

$$g_{,s}(0) = g_{,s}(1) = 0. \tag{34}$$

[4] As already mentioned in [1], the differential equations for the shape of the beam are integrable. With these particular boundary conditions, however, analytical approaches of the problem lead to a set of implicit equations, which do not simplify the resolution.

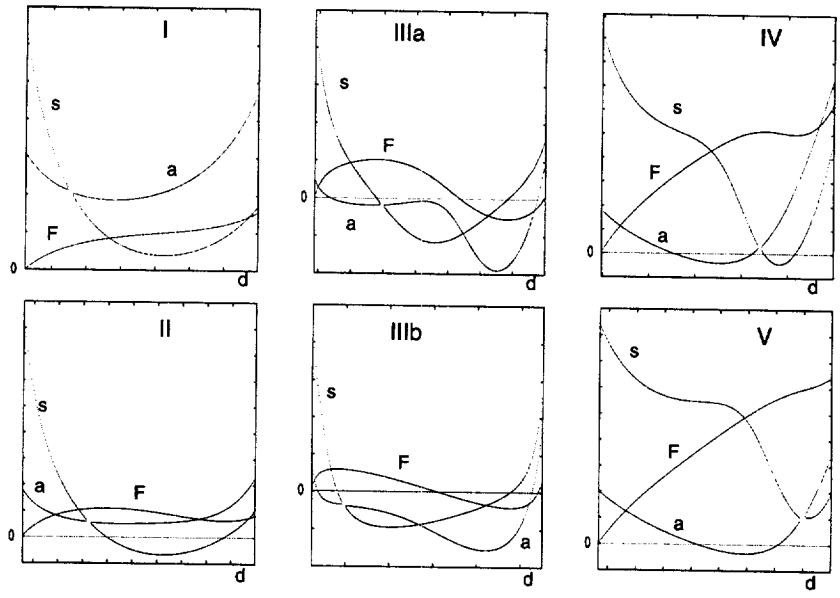

Fig. 3. Plots of the force $F(d)$ (curve F) and the first two eigenvalues $\omega^2(d)$ (curves a and s – corresponding to an asymmetric and a symmetric perturbation, respectively) for different values of l and α. In each figure, the horizontal axis corresponds to the displacement $d \equiv h_0 - h_1$, where h_0 is the height of the mid-point in the absence of external force. Note that the functions F and ω^2 have arbitrary units.

This eigenvalue problem can be solved numerically using a three dimensional shooting method, similar to the one already described. It is clear that each eigenmode is determined up to a constant factor. So, one can impose the initial conditions $\phi(0) = f_{,s}(0) = g_{,s}(0) = 0$, together with $\phi_{,s}(0) = 1$. We have then three initial guesses $f(0)$, $g(0)$ and ω^2 which have to be varied until the end boundary conditions $\phi(1) = f_{,s}(1) = g_{,s}(1) = 0$ are satisfied. The symmetric configuration of the beam is stable (unstable) if ω^2 is found positive (negative).

Instabilities are found for nontrivial solutions of $\omega^2 = 0$. The numerical results are summarized in Fig. 3. Figs. 3, I–V correspond to different values of the length l and of the clamping angle α. In each figure, the horizontal axis corresponds to the displacement $d \equiv h_0 - h$, where h_0 is the height of the mid-point in the absence of external force. The curves labelled F represent the force $F(d)$ needed to be applied to ensure the position h to the mid-point. We also plot the first two eigenvalues $\omega^2(d)$. The curves labelled a represent the eigenvalue ω^2 that corresponds to an asymmetric perturbation. That is, the eigenvalue associated with a perturbation that satisfies $\phi(1/2) \neq 0$. On the other hand, the curves labelled s represent the eigenvalue ω^2 of a symmetric perturbation ($\phi(1/2) = 0$). If the curve a becomes negative first, we expect that the corresponding asymmetric perturbation leads to an asymmetric deviation of the arch. Otherwise, if the curve s becomes negative first, we expect that the symmetric perturbation leads to the symmetric plunging of the arch. Note that there is always an anticrossing between these two first eigenmodes. This feature is responsible for a rich variety of situations. One can distinguish five different phases:

- Part I: $\alpha = 120°$ and $l = 0.7$. The eigenvalues are always positive while the force increases for all values of d. We have here a stable situation, where the elastic arch is deformed continuously as the applied force increases.
- Part II: $\alpha = 100°$ and $l = 0.6$. The asymmetric eigenvalue remains positive while the symmetric one, after an anticrossing, gets unstable. The force increases until the point of instability, it decreases in the unstable region and starts to increase again for positive values of the symmetric eigenvalue. In fact, the sign of the symmetric eigenvalue is always equal to the sign of the derivative of the force. In this case, the arch starts to be deformed as

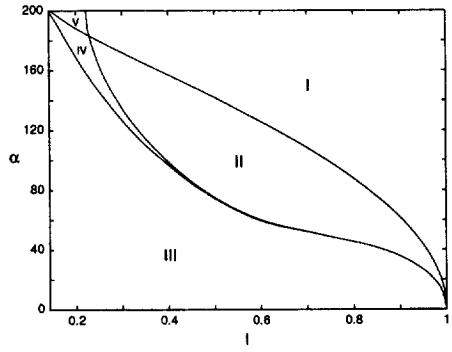

Fig. 4. Phase diagram of the distinct regions on an l–α plane in which different types of instability occur, obtained by the linear stability analysis of the symmetric configuration. The labels correspond to the regions described in the text.

the force increases. For a critical force, a first-order transition occurs. The arch plunges directly to distant values of d, at a certain point with the same critical force.

- Part IIIa and IIIb: $\alpha = 60°$ and $l = 0.4$; $\alpha = 20°$ and $l = 0.8$. The asymmetric eigenvalue becomes rapidly negative. The symmetric solution is unstable for almost all values of d. In both cases, we expect an asymmetric solution for a certain critical force. This instability would correspond to a second-order transition, with a continuity of deformed symmetric and asymmetric elastic arches.
- Part IV: $\alpha = 180°$ and $l = 0.2$. The asymmetric and symmetric eigenvalues have negative values in distinct different regions of the coordinate d. For a first critical force, the symmetric arch solution has an asymmetrical instability. There is a second critical force for which it becomes stable again. Finally, for a third critical force it plunges symmetrically.
- Part V: $\alpha = 200°$ and $l = 0.2$. In this case, only the asymmetric eigenvalue has negative values. The symmetric arch passes through an asymmetric instability. For a second critical force, the symmetric arch becomes stable again. Afterwards, it suffers a continuous deformation as the applied force F is increased.

The global behavior of the dynamic stability of the symmetric arch solutions can be summarized in a phase diagram spanning all values of α and l (see Fig. 4). The different lines plotted, calculated numerically, divide the plan into the five regions described above.

Note that our study, based on the linear stability analysis of the symmetric solution, predicts the instabilities of the symmetric arch. Nevertheless, if a transition occurs, the linear stability analysis can only guess the final equilibrium form of the arch. Our guess is made by observing the symmetry or asymmetry of the perturbation that was responsible for this instability. The correct behavior of the beam should be obtained by the complete nonlinear problem.

4. Stable solutions found by the energy minimization method

Since the previous study has revealed a rather rich structure, we have decided to determine all the final static solutions of the problem, by using an energy minimization algorithm. Even if it implies more careful and larger numerical calculations, this method has the advantage to always select a stable solution. [5] As we increase the applied force F at the mid-point of the elastica, we can follow the symmetric or asymmetric behavior of the deformed arch,

[5] The minimum of the energy seems to be, in this case, equivalent to a stable solution in a dynamic sense.

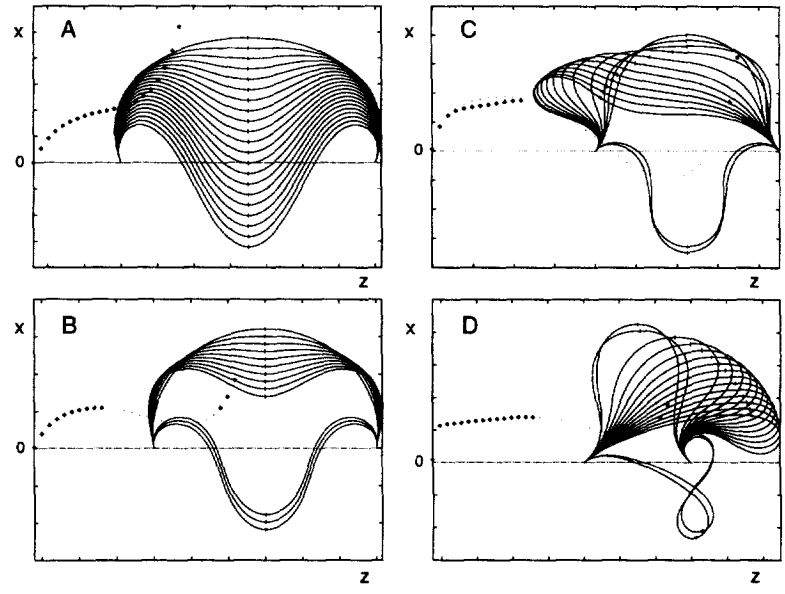

Fig. 5. The deformations of the elastic arch when the applied force at the mid-point is increased, for different values of the control parameters α and l. Bold points indicate the values of the corresponding applied forces F as a function of the displacement $d \equiv h_0 - h$.

regardless of its instabilities. By contrast with the shooting method, this method does not *block* itself near an instability of first order.

Using the two Lagrange multipliers λ_1 and λ_2, we can write the total static energy of the arch as (see Section 2):

$$E_{\text{tot}} = \frac{1}{2}\int_0^1 \theta_{,s}^2(s)\,\mathrm{d}s - \lambda_1 \int_0^1 \cos\theta(s)\,\mathrm{d}s - \left(\lambda_2 - \frac{F}{2}\right)\int_0^{1/2} \sin\theta(s)\,\mathrm{d}s - \left(\lambda_2 + \frac{F}{2}\right)\int_{1/2}^1 \sin\theta(s)\,\mathrm{d}s. \tag{35}$$

To solve numerically this problem, we have used a finite element space for the function $\theta(s)$, with boundary conditions $\theta(0) = -\theta(1) = \alpha$. For each couple of values λ_1 and λ_2, minimization of the total energy E_{tot} is carried out. λ_1 and λ_2 are fixed such that the integral constraints (10) are satisfied.

Within this method, we can follow the deformation of the arch as we increase the applied force F. In Fig. 5, we have represented the deformations of the arch, for different values of the increasing force. We have also represented the values of F as a function of the displacement $d \equiv h_0 - h$. As shown in these figures, we can characterize four different situations, according to certain values of l and α:

- Part A: $\alpha = 120°$ and $l = 0.7$. The arch is deformed continuously, as we increase the force. Because the arch remains symmetric, we have here the situation described in part I, of the previous section.
- Part B: $\alpha = 100°$ and $l = 0.6$. At a certain critical force, we have a first-order transition, and the arch plunges. This corresponds to the situation described in part II of Section 3.
- Part C: $\alpha = 60°$ and $l = 0.45$. When the force reaches a first critical value, we have a second-order symmetric–asymmetric transition. At a second critical force, there is a first-order transition. The arch plunges from the asymmetric configuration into a symmetric one.

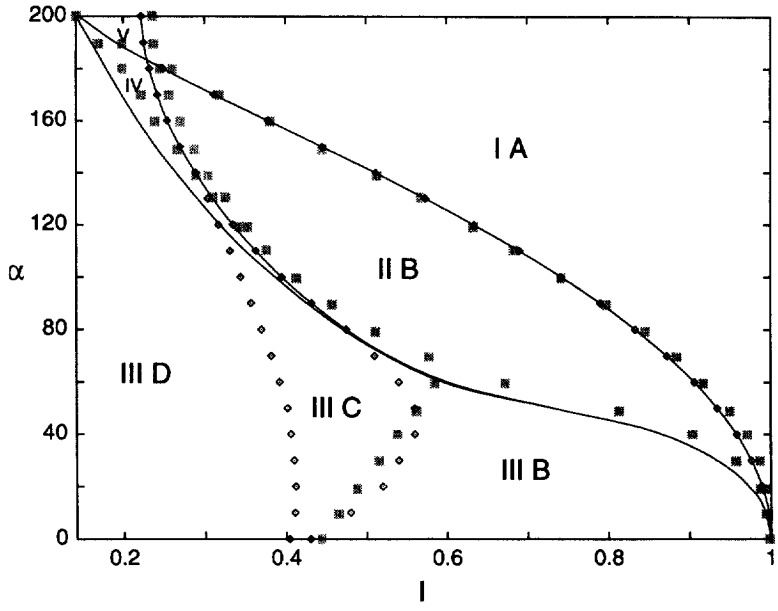

Fig. 6. Phase diagram of the distinct regions on an l–α plane in which different types of instability occur. The diamond-shape points separating the regions A–D represent the results of the minimization of the static energy. The results of the linear stability analysis are represented by continuous lines (separating regions I–V). The gray squares correspond to Pippard's experiment [1].

– Part D: $\alpha = 40^\circ$ and $l = 0.3$. The behavior of the arch begins in the same way as in the previous case. However, the arch does not come back to the symmetric forms. Within this mathematical model, it reaches unphysical asymmetric deformations. At a certain critical force, there is a first-order transition, and the arch plunges to an asymmetric solution, with a self-intersection.

The distinct regions of the evolution of the arch patterns were numerically calculated, and their phase diagram is represented in Fig. 6. For comparison, the results of the linear stability analysis and the experimental data [1] are also shown.

5. Discussion

In Fig. 6, we show the phase diagram of the distinct regions on an l–α plane in which different types of instability occur. The diamond-shape points represent the results of the minimization of the static energy. The results of the linear stability analysis are represented by continuous lines. The gray squares correspond to Pippard's experiment [1]. We have labelled the different regions with Roman numbers I–V (corresponding to the results of the linear stability analysis, see Section 3) and capital letters A–D (corresponding to the results of energy minimization, see Section 4).

There is a very good agreement between our numerical results and the experimental data. All experimental phases are found by our elastica model. However, it was necessary to combine both theoretical methods in order to describe the different experimental observations.

In fact, there are several differences in the results of the dynamic linear stability analysis and the energy minimization. Such differences give rise to the complexity of the l–α phase diagram. Let us examine in detail each part of the phase diagram.

The plunging symmetric phases predicted by the linear stability analysis (II) and the minimization (B) do not coincide. In the region labelled (II B), both methods give the same result. The linear stability analysis shows that at a certain critical force, the symmetric arch becomes dynamically unstable with respect to symmetric perturbations. The minimization method also leads to a symmetric plunging transition at the same critical force. On the contrary, in the region labelled (III B), the linear stability analysis shows an asymmetric instability. However, the minimization of the static energy shows a symmetric plunging at exactly the same threshold. Since there are no stable asymmetric solutions, the arch will plunge symmetrically. Indeed, the region (III B) coincides with the region called B_u in Pippard's experiment [1].

In regions (III C) and (III D), both approaches agree again. However, the dynamical stability analysis has been done around the symmetric arch only. The evolution of the asymmetric behavior, achieved by a minimization method, enables us to differentiate between these two regions. Region (D) is not observed experimentally. This region goes beyond the physical limits of the experiment and the mathematical model reaches unphysical deformations.

In regions (IV) and (V), after a critical force, F_1, we have obtained asymmetrical solutions (see Fig. 5D) with the minimization method. For this, we have followed the asymmetric evolution of the deformed arch, as we increased the applied force. Remember that the linear stability analysis has shown that, after F_1, the symmetric arch is destabilized by an asymmetric mode (confirmed by the minimization method), but it revealed also a second threshold, F_2, where the symmetric solution becomes stable again. By following the asymmetric solutions in the minimization method, we have never recovered the symmetric arch, even above F_2. It is perhaps a case of metastability, since Pippard [1] has observed experimentally these two regions, by imposing initial symmetric forms.

Finally, we underline the necessity of both theoretical methods to describe completely the experimental results. The linear stability analysis allows the determination of the instabilities of the arch, together with the associated linear dynamic modes. If a transition occurs, this method does not predict the final equilibrium form of the arch. The energy minimization method allows the determination of the instabilities of the arch, and the corresponding final states of equilibrium. However, this method only solves the static problem. It has no information about the dynamical behavior of the elastic arch.

6. Conclusion

Pippard has shown experimentally that an elastic beam, fixed at both ends, loaded at its center, exhibit a rather rich phase diagram. He has interpreted it qualitatively in terms of *catastrophe theory* [2]. We have obtained this phase diagram by solving numerically the *elastica* model, with suitable constraints. In order to describe the different experimental observations, it was necessary to combine a linear dynamical stability analysis with a minimization of the static energy.

This very simple model of beam explains perfectly the physical behavior in each part of the diagram. Moreover, the numerical and experimental results coincide in their main characteristics without adjustable parameters. This shows that, even in situations of strong nonlinear behavior, the simple *elastica* model remains valid.

Acknowledgements

We are grateful to E. Corvera Poiré, Y. Couder and W. Krauth for helpful discussions and critical comments.

References

[1] A.B. Pippard, The elastic arch and its modes of instability, Eur. J. Phys. 11 (1990) 359–365.
[2] J.M.T. Thompson, Instabilities and Catastrophes in Science and Engineering, Wiley, Chichester, 1982, p. 13.
[3] A.E.H. Love, Mathematical Theory of Elasticity, Cambridge University Press, Cambridge, 1927.
[4] P. Patrício, M. Ben Amar, Y. Couder, in preparation.
[5] A.V. Pogorelov, Bending of Surfaces and Stability of Shells, American Mathematical Society, Providence, RI, 1985.
[6] S.S. Antman, Nonlinear Problems of Elasticity, Springer, New York, 1995.
[7] R.E. Caflisch, J.H. Maddocks, Nonlinear dynamical theory of the elastica, Proc. R. Soc. Edinburgh A 99 (1984) 1–24.
[8] B.D. Coleman, E.H. Dill, Flexure waves in elastic rods, J. Acoust. Soc. Am. 91 (1992) 2663–2673.
[9] A. Goriely, M. Tabor, Nonlinear Dynamics of Filaments: I. Dynamical Instabilities, II. Nonlinear Analysis, Physica D 105 (1997) 20–61.